Optics Letters

# Single-shot lensfree on-chip quantitative phase microscopy with partially coherent LED illumination

Yang Chen,[1,2,3] Xuejuan Wu,[1,2,3] Linpeng Lu,[1,2,3] Jiahao Wei,[1,2,3] Yumin Wu,[1,2,3,4] Qian Chen,[1,3,5] and Chao Zuo[1,2,3,*]

[1]Smart Computational Imaging Laboratory (SCILab), School of Electronic and Optical Engineering, Nanjing University of Science and Technology, No. 200 Xiaolingwei Street, Nanjing, Jiangsu Province 210094, China
[2]Smart Computational Imaging Research Institute (SCIRI) of Nanjing University of Science and Technology, Nanjing, Jiangsu Province 210019, China
[3]Jiangsu Key Laboratory of Spectral Imaging & Intelligent Sense, Nanjing, Jiangsu Province 210094, China
[4]BGI-Shenzhen, Shenzhen 518083, China
[5]e-mail: chenqian@njust.edu.cn
*Corresponding author: zuochao@njust.edu.cn

Received 7 September 2022; revised 16 October 2022; accepted 26 October 2022; posted 27 October 2022; published 15 November 2022

**We propose a single-shot lens-free phase retrieval (SSLFPR) method in a lens-free on-chip microscopy (LFOCM) system based on a partially coherent light emitting diode (LED) illumination. The finite bandwidth (~23.95 nm) of LED illumination is divided into a series of quasi-monochromatic components according to the LED spectrum measured by a spectrometer. When the "virtual wavelength scanning" phase retrieval method is combined with the dynamic phase support constraint, the resolution loss caused by the spatiotemporal partial coherence of the light source can be effectively compensated. At the same time, the nonlinearity characteristics of the support constraint help to further improve the imaging resolution, accelerate the convergence of the iteration process, and greatly eliminate the artifacts. Based on the proposed SSLFPR method, we demonstrate that the phase information of samples (including phase resolution target and polystyrene microspheres) illuminated by a LED can be accurately retrieved based on one single diffraction pattern. The SSLFPR method has a half-width resolution of 977 nm across a large field-of-view (FOV) of 19.53 mm$^2$, which is 1.41 × the resolution of the conventional approach. We also imaged living Henrietta Lacks (HeLa) cells cultured *in vitro*, further demonstrating the real-time single-shot quantitative phase imaging (QPI) capability of SSLFPR for dynamic samples. Given its simple hardware, high throughput, and single-frame high-resolution QPI capability, SSLFPR is expected to be adopted in a wide range of biological and medical applications.** 

https://doi.org/10.1364/OL.474992

In recent years, there has been increasing demand for high-throughput imaging of the subcellular structure in biological samples, especially in the fields of cell biology, digital pathology, and high-throughput drug screening [1]. Limited by the inherent trade-off between objective magnification and field-of-view (FOV), conventional microscopes have difficulty in achieving high-resolution and wide FOV simultaneously. The limitations of the FOV and the resolution can be partially overcome by using the high-precision scanning platform and image stitching algorithm. But the system becomes more complex, and the recording and calculating processes become more time-consuming, which is unsuitable for dynamic imaging.

The emergence and rapid development of lens-free on-chip microscopy (LFOCM) in recent years has provided a promising solution to the above problem [2–8]. In a typical LFOCM system, in-line holograms over the full FOV are recorded for phase reconstruction with all lenses removed and the sample placed close to the sensor. The resolution of a typical LFOCM system is limited by the sampling frequency and coherent diffraction limit. Considering its effective numerical aperture (NA) is close to unity, the pixel-size may be the main factor affecting the imaging resolution. Therefore, in most lens-free imaging systems, it has been demonstrated that small pixel sensors and high coherence laser sources, combined with many pixel super-resolution methods, including sub-pixel lateral translation of image sensors [9], active parallel plate scanning [10], sample-to-sensor distances scanning [11], and multi-wavelength scanning [12,13] are used to break through the limitation of sampling frequency. Compared with the laser, partially coherent illumination is particularly useful in the field of optical microscopic imaging, providing a speckle-free image as well as higher throughput. In addition, the light emitting diode (LED) is small and cost-effective, which is conducive to the miniaturization of the lens-free microscope. Therefore, partially coherent LED [14,15] has been used to improve the imaging quality in recent years. However, according to the lens-free imaging resolution theoretical analysis proposed by our group [6], the lack of spatio-temporal coherence of LED causes the diffraction of high-frequency information to mix into the low-frequency regions, replacing the sampling frequency as the main factor limiting the imaging resolution. To solve the above problems and obtain a higher resolution, some methods have been explored to compensate for the resolution loss caused by the partially coherence of LED [16,17]. However, they only image sparse samples

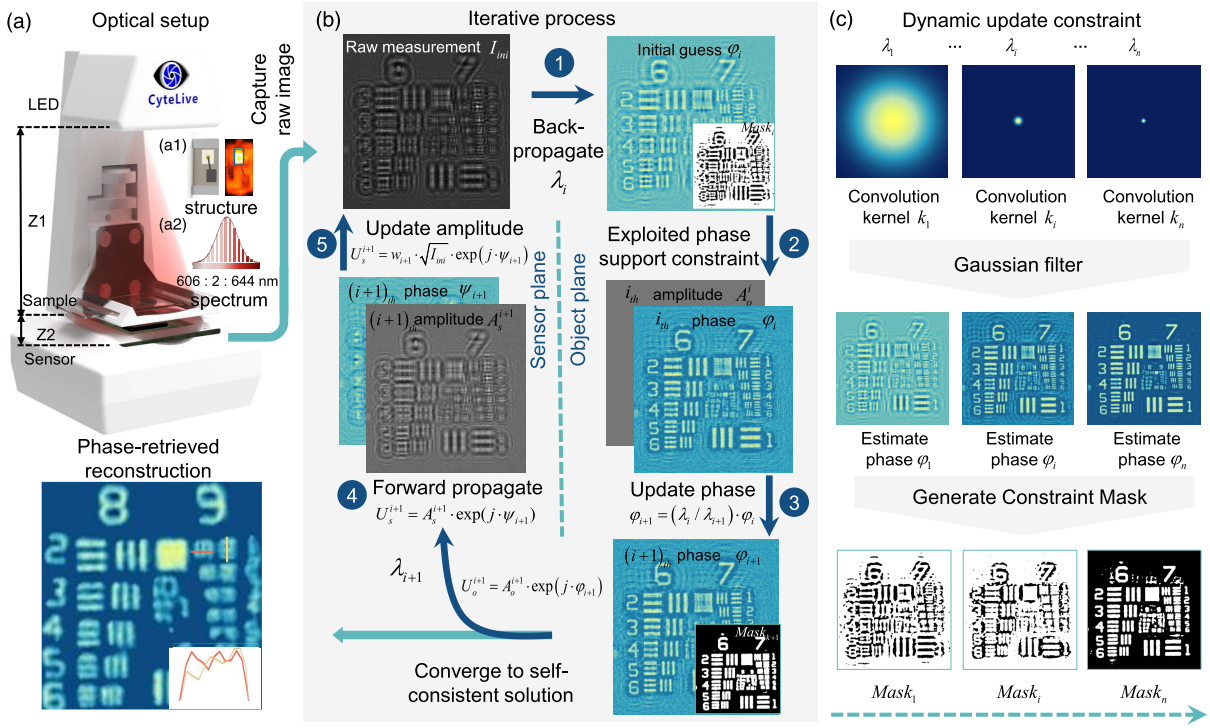


**Fig. 1.** Flowchart of the LFOCM single-shot phase retrieval algorithm.

or simple grating. Therefore, the single-frame phase recovery technology of LFOCM and the long-term dynamic quantitative phase imaging (QPI) observation of biological samples have not been reported so far.

In this Letter, we propose a single-shot lens-free phase retrieval (SSLFPR) method based on partially coherent LED illumination. Without using additional pinholes and filters, it directly obtains fast real-time single-shot dynamic QPI results with a high signal-to-noise ratio (SNR) in conventional LFOCM systems based on LED illumination.

The overview flowchart of SSLFPR is illustrated in Fig. 1. Figure 1(a) depicts the configuration of our single-shot phase retrieval LFOCM system. In our LFOCM system, a partially coherent LED is used to mitigate resolution loss caused by speckle and reflection interference noise (wavelength ~ 632 nm, bandwidth ~ 23.95 nm, emitting area ~ 0.0091 $mm^2$). After propagating ~ 150 mm ($Z_1$), the partially coherent light interacts with the sample to generate one hologram to be recorded by an industrial-grade CMOS sensor (pixel size ~ 0.9 μm, 5664 × 4256, Jiangsu Team-one Intelligence Technology Co. LTD.) placed close to the sample ($Z_2$ ~ 0.5 mm, satisfying near-field diffraction theory). It should be noted that the refractive index of our samples in the 604–652 nm range approximated as a constant ($\Delta n$<0.35%) [18]. Therefore, we ignore the effect of dispersion. Since $Z_1 \gg Z_2$, the illumination wavefront can be approximated as a plane wave. According to Zhang's spatio-temporal coherence resolution derivation formulas [Ref. 6, Eqs. (10) and (12)], substituting the specific parameters, we can get that the resolution limits of spatial and temporal coherence are $q_s \approx 266$ nm and $q_t \approx 1350$ nm, respectively. Considering that the resolution loss caused by spatial coherence has exceeded the pixel size, we only discuss the influence of temporal coherence. If polychromatic light is used for illumination, the diffraction pattern recorded in the defocus plane can be regarded as the result of the superposition of the intensity of many diffraction images of the same object nearby. This dispersion effect enhances with the defocusing distance increased, i.e., $I_{\text{ini}} = w_1 I_1 + w_2 I_2 + \ldots + w_i I_i$, where $w_i$ is the weighting factor of sub-wavelength. The factor $w_i$ is determined by the specific spectrum of the LED. Obviously, the superposition of uncorrelated diffuse spots will produce a smoothing effect, resulting in the attenuation or even loss of high-frequency details. According to the above imaging model, the LED with a spectral width of $\Delta\lambda \approx 23.95$ nm is divided into 20 monochromatic illumination sub-wavelengths. We have selected a segmentation interval of 2 nm through many simulation experiments, which can ensure the imaging effect without increasing the computing time. Then the phase iteration method is implemented according to the divided sub-wavelengths. The main process is as follows.

**Process 1: Implement dynamic phase constraints.** Based on the captured hologram $I_{ini}$, the complex amplitude $U_s^i$ is propagated to the object plane using the angular spectrum method. Apply Gaussian filtering to the phase $\varphi_i$. The width of convolution kernel is initialized to $s$ (set to five pixels in the first iteration, reduced by 2% each time). The threshold value of the image is obtained using maximizing interclass variance methods for binarization to obtain $\text{Mask}_{i+1}$. The dynamic constraint $\text{Mask}_i$ can enable iterative convergence to the unique solution, among many other possibilities, based on the measured hologram intensity and the estimated object support [19].

**Process 2: Iterative phase retrieval.** The complex amplitude $U_s^i$ is propagated back to the object plane to get $U_o^i = A_o^i \exp(j\,\varphi_i)$. Apply the constraint to update the phase $\varphi_i' = \varphi_i\ \text{Mask}_i$, which is scaled as $\varphi_{i+1} = \varphi_i' \lambda_i / \lambda_{i+1}$ when the wavelength changes. Then, apply uniform intensity constraint to the amplitude $A_o^{i+1} = \text{ave}\left(A_o^i\right)$, where ave(·) is aimed to obtain the average. Finally, propagate $U_o^{i+1}$ forward to the sensor plane and update the complex amplitude $U_s^{i+1} = \sqrt{w_{i+1} I_{ini}} \exp(j\,\psi_{i+1})$ with

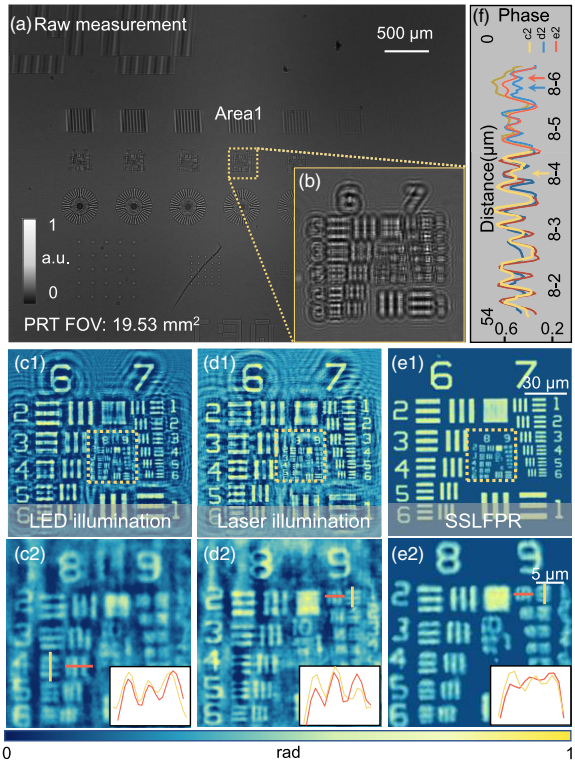


**Fig. 2.** Experimental results of quantitative phase resolution target (PRT). (a) Raw hologram of the full FOV. (b) The enlarged region corresponds to the yellow boxed area. (c1)–(e1) Reconstruction phases using back-propagation method with LED and laser illumination and using SSLFPR. (c2)–(e2) Enlarged regions corresponding to the boxed areas in (c1)–(e1) and phase values along the yellow and red lines. (f) Comparison of phase values of Group 8 Elements 2–6.

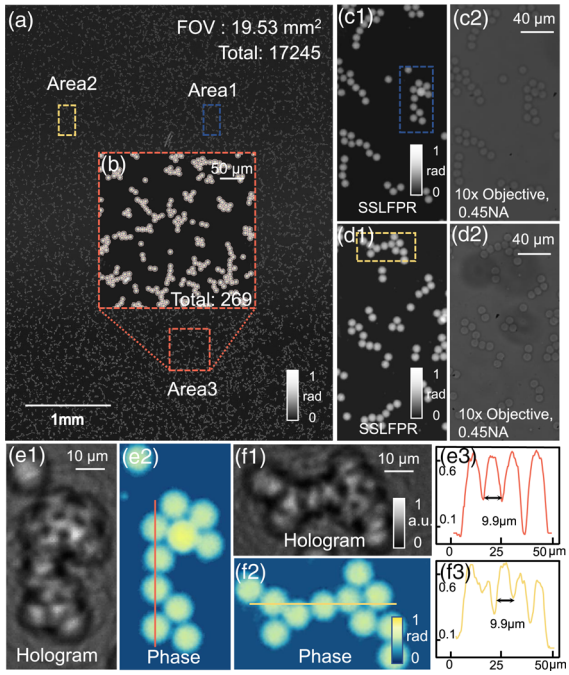


**Fig. 3.** Experimental result of polystyrene microsphere sample (10 μm). (a) Reconstruction phase of the full FOV. (b) Enlarged region of the counting result corresponding to Area3. (c1),(d1) Reconstruction phases corresponding to Area1 and Area2. (c2),(d2) Intensities taken with a $10 \times 0.45$ NA microscope objective. (e1),(f1) In-line holograms corresponding to the boxed area in (c1) and (d1). (e2),(f2) Reconstructed phases corresponding to (e1) and (f1). (e3),(f3) Phase values along the yellow and red lines in (e2) and (f2).

the hologram $I_{ini}$. Then, the iteration is repeated until the change of mean square error (MSE) is less than 1%. To demonstrate the improvement effect of SSLFPR on the enhancement of imaging resolution and SNR, we image the quantitative PRT. Figure 2(a) shows an in-line hologram across the full FOV (19.53 $mm^2$). The inset [Fig. 2(b)] shows an enlarged region corresponding to the boxed area in Fig. 2(a), containing a typical set of resolution elements. Figures 2(c1) and 2(d1) show the reconstructed phases using the back-propagation method based on the LED and laser illumination, respectively. The resolution based on the laser is limited by the low single-noise-ratio caused by twin image. Figure 2(e1) is the retrieved phase using SSLFPR. The enlarged areas in Figs. 2(c1)–2(e1) and the phase value alone the yellow and red lines are shown in Figs. 2(c2)–2(e2) and insets. According to the insets in Figs. 2(c2) and 2(d2), the half-width resolution of the retrieved phase based on the LED illumination is 1.381 μm (Group 8 Element 4), which does not match the resolution based on laser illumination (Group 9 Element 1, 0.977 μm). According to Fig. 2(e2), the half-pitch resolution using SSLFPR is improved to 0.977 μm (Group 9 Element 1), which is 1.41× the resolution of the conventional single-shot method. Figure 2(f) is the spatial profile distributions of Group 8 Elements 2–6 which shows the loss of resolution based on the LED illumination.

We imaged a polystyrene microsphere sample (10 μm) to demonstrate the accurate QPI capability of SSLFPR. Figure 3(a) shows the reconstructed phase of the full FOV (19.53 $mm^2$). According to the counting algorithm, the number of polystyrene microspheres across the full FOV is 17 245. The schematic diagram of the counting result of Area3 is shown in the inset [Fig. 3(b)]. Figures 3(c1) and 3(d1) are enlarged regions of reconstruction phase corresponding to Area1 and Area2 in the full FOV, respectively. Figures 3(c2) and 3(d2) are intensity image captured by a $10 \times 0.45$ NA microscope objective. The reconstructed microsphere phase using SSLFPR matches well with the bright field map. We select the yellow and blue boxed areas in Figs. 3(c1) and 3(d1) for analysis. Figures 3(e1) and 3(f1) are the holograms corresponding to the above regions. The reconstruction phase of Figs. 3(e1) and 3(f1) is shown in Figs. 3(e2) and 3(f2). Figures 3(e3) and 3(f3) show the phase values along the yellow and red lines. The interval between two adjacent peaks is roughly 9.9 μm, which is consistent with the theoretical value of 10 μm.

Finally, we demonstrate the wide-field dynamic QPI capability of SSLFPR by long-term real-time imaging of living Henrietta Lacks (HeLa) cells. Thanks to the compactness of our system, it fits easily inside a cell culture incubator for *in situ* cell monitoring. In Visualization 1, we provide a real-time video of HeLa cell across the full FOV recovered by SSLFPR with several zoomed-in regions.

The reconstruction phase and the hologram across the full FOV at time 00:01:00 in this video are shown in Fig. 4(a). In Figs. 4(b1)–4(b5), we selected a pair of cells corresponding to Area2 in Fig. 4(a) to study their sequential motion.

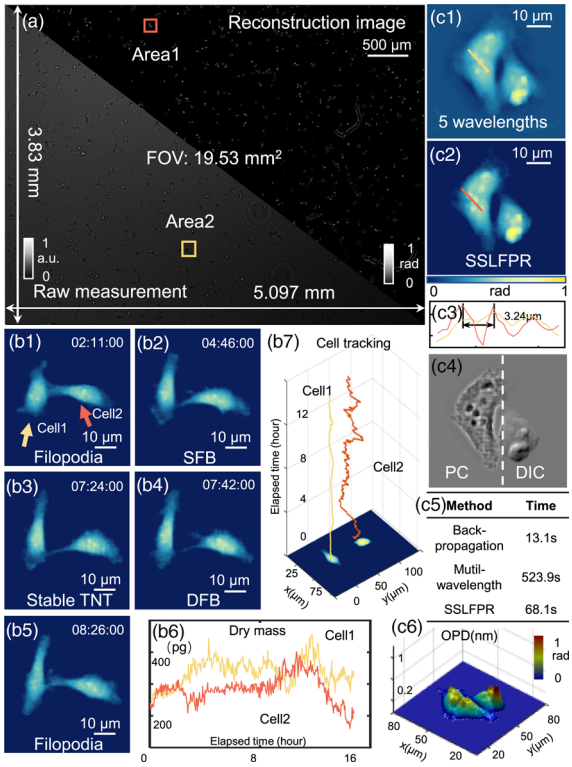


**Fig. 4.** Dynamic phase imaging of HeLa cells in culture (Visualization 1). (a) Hologram and phase of the full FOV. (b1)–(b5) Five selected time-lapse phase images of Area2. (b6),(b7) Dry mass changes of two cells over time and dynamic tracking. (c1) Reconstructed phase using conventional multi-wavelength phase retrieval method based on five LEDs. (c2) Reconstructed phase using SSLFPR. (c3) Phase values along the yellow and red lines in (c1) and (c2). (c4) Simulated phase-contrast image (PC) and simulated differential interference contrast (DIC) image. (c5) Calculation schedule of the FOV (5664 × 4256) for each method. (c6) Three-dimensional (3D) rendering.

Figures 4(b1)–4(b5) show the formation and disappearance process of tunneling nanotubes (TNTs). The high-resolution phase images demonstrated the cell morphology at different stages of the TNTs generation process, including single filamentary bridges [Fig. 4(b2)], stable TNTs [Fig. 4(b3)] and double filamentary bridges [Fig. 4(b4)]. Figures 4(b6) and 4(b7) show the change curve of cell dry mass and the trajectories of the two cells in Fig. 4(b1). Figures 4(c1) and 4(c2) are the phases (reconstructed by the traditional multi-wavelength method [13] and SSLFPR) corresponding to Area1 in Fig. 4(a), respectively. Figure 4(c3) shows the peak-to-valley features in Figs. 4(c1) and 4(c2), which corresponds to the distance of ~ 3.24 μm. Based on the retrieved quantitative phase, the PC, and DIC image can be obtained computationally without resorting to additional hardware, as shown in Fig. 4(c4). As shown in Fig. 4(c5), SSLFPR reduced much computation time compared with multi-wavelength methods. Figure 4(c6) shows the pseudo-3D morphology (an accumulation of refractive index over the cell thickness). SSLFPR only needs one single hologram to perform wide-field quantitative phase recovery with high resolution and high SNR.

In summary, we propose a new single-shot phase retrieval method for the LFOCM system based on partially coherent LED illumination. With one hologram, SSLFPR combined with an incoherent imaging model, achieves long-term dynamic QPI imaging of unstained living samples using dynamic phase support constraints and virtual multi-wavelength algorithms. The experimental results show that SSLFPR achieves a half-pitch resolution of 977 nm across the full FOV of 19.53 mm$^2$, which is 1.41× the conventional single-shot method based on LED illumination. Compared with the multi-wavelength method, SSLFPR makes the imaging speed 10× faster without sacrificing the imaging resolution and SNR. Live-cell experiments demonstrate that the proposed method provides a high-resolution, high-SNR, and high-throughput real-time imaging tool for long-term cellular in situ monitoring *in vitro*. However, for dense objects without obvious boundaries, such as highly adherent cell groups, our method is also difficult to image objects inside clustered areas, which is the direction to be improved later.

**Funding.** National Natural Science Foundation of China (61905115, 62105151, 62175109, U21B2033); Leading Technology of Jiangsu Basic Research Plan (BK20192003); Youth Foundation of Jiangsu Province (BK20190445, BK20210338); Fundamental Research Funds for the Central Universities (30920032101); Open Research Fund of Jiangsu Key Laboratory of Spectral Imaging & Intelligent Sense (JSGP202105, JSGP202201); Open project of BGI-Shenzhen (BGIRSZ20210011).

**Disclosures.** The authors declare no conflicts of interest.

**Data availability.** Data underlying the results presented in this paper are not publicly available at this time but may be obtained from the authors upon reasonable request.

## REFERENCES

1. H. R. Maricq and E. Carwile LeRoy, Arthritis Rheum. **16**, 619 (1973).
2. A. Ozcan and U. Demirci, Lab Chip **8**, 98 (2008).
3. G. Zheng, S. A. Lee, Y. Antebi, M. B. Elowitz, and C. Yang, Proc. Natl. Acad. Sci. **108**, 16889 (2011).
4. W. Zhang, L. Cao, G. Jin, and D. Brady, Appl. Opt. **57**, A164 (2018).
5. H. Zhang, Z. Bian, S. Jiang, J. Liu, P. Song, and G. Zheng, Opt. Lett. **44**, 1976 (2019).
6. J. Zhang, J. Sun, Q. Chen, and C. Zuo, IEEE Trans. Comput. Imaging **6**, 697 (2020).
7. Y. Ma, J. Wu, S. Chen, and L. Cao, Opt. Express **30**, 15266 (2022).
8. S. Jiang, C. Guo, Z. Bian, R. Wang, J. Zhu, P. Song, P. Hu, D. Hu, Z. Zhang, K. Hoshino, B. Feng, and G. Zhenga, Biosens. Bioelectron. **196**, 113699 (2022).
9. Y. Wu, Y. Zhang, W. Luo, and A. Ozcan, Sci. Rep. **6**, 28601 (2016).
10. J. Zhang, Q. Chen, J. Li, J. Sun, and C. Zuo, Opt. Lett. **43**, 3714 (2018).
11. A. Greenbaum, Y. Zhang, A. Feizi, P.-L. Chung, W. Luo, S. R. Kandukuri, and A. Ozcan, Sci. Transl. Med. **6**, 267ra175 (2014).
12. P. Bao, F. Zhang, G. Pedrini, and W. Osten, Opt. Lett. **33**, 309 (2008).
13. X. Wu, J. Sun, J. Zhang, L. Lu, R. Chen, Q. Chen, and C. Zuo, Opt. Lett. **46**, 2023 (2021).
14. D. Tseng, O. Mudanyali, C. Oztoprak, S. O. Isikman, I. Sencan, O. Yaglidere, and A. Ozcan, Lab Chip **10**, 1787 (2010).
15. Y. Fan, J. Li, L. Lu, J. Sun, Y. Hu, J. Zhang, Z. Li, Q. Shen, B. Wang, R. Zhang, Q. Chen, and C. Zuo, PhotoniX **2**, 19 (2021).
16. I. Sencan, A. F. Coskun, U. Sikora, and A. Ozcan, Sci. Rep. **4**, 3760 (2015).
17. S. Feng and J. Wu, Opt. Express **25**, 24735 (2017).
18. D. Marcuse, *Light transmission optics* (New York, 1982).
19. S. Marchesini, H. He, H. N. Chapman, S. P. Hau-Riege, A. Noy, M. R. Howells, U. Weierstall, and J. C. Spence, Phys. Rev. B **68**, 140101 (2003).